# Understanding chiral proton organocatalysis using cinchonium derivatives

Fernando Auria-Luna,[†] Eugenia Marqués-López,[†] M. Concepción Gimeno,[ξ] Juan V. Alegre-Requena,*[,ξ] and Raquel P. Herrera*[,†]

[†] Laboratorio de Organocatálisis Asimétrica, Departamento de Química Orgánica, Instituto de Síntesis Química y Catálisis Homogénea (ISQCH) CSIC-Universidad de Zaragoza, C/ Pedro Cerbuna 12, 50009 Zaragoza, Spain.

[ξ] Departamento de Química Inorgánica, Instituto de Síntesis Química y Catálisis Homogénea (ISQCH) CSIC-Universidad de Zaragoza, C/ Pedro Cerbuna 12, 50009 Zaragoza, Spain.

**ABSTRACT:** This work presents a detailed mechanistic study of a quininium-catalyzed aza-Michael reaction, providing essential information for the development of reactions in chiral proton organocatalysis (CPO). The use of cinchona derivatives as chiral proton catalysts demonstrates their potential beyond their conventional roles as base-promoted and phase-transfer catalysts. Competitive reaction pathways are studied using density functional theory (DFT), wavefunction theory, and microkinetic simulations. Additionally, theoretical studies are complemented with experimental titration and kinetic techniques to verify the intrinsic details of the reaction. The mechanistic study reveals a complex hydrogen bond network formed in the rate- and selectivity-determining step (hydrazide addition), involving four noncovalently attached components that favor a more efficient substrate docking in the *R* transition state. Notably, while counteranions are often considered innocent reaction components, carboxylic anions are crucial in understanding reaction yield and enantioselectivity, as they act as nucleophile-activating bases. Overall, this study introduces cinchonium derivatives as new options for CPO and provides a thorough mechanistic analysis that may be critical in expanding this underdeveloped type of catalysis.

## INTRODUCTION

Chiral proton organocatalysis (CPO) is a field that relies on substrate activation through ionic hydrogen bonds.[1] This area, which is often included in the broader category of Brønsted acid catalysis,[2-6] encompasses chiral cationic catalysts that bear protonated nitrogen atoms serving as hydrogen-bond donors, preserving the protonation state after performing the catalytic cycles with no need to add any external reagent.[1] The increased acidity of charged hydrogen donors provides an advantage in the activation of electrophiles, as proton acidity is greater than that of common motifs used in organocatalysis, such as (thio)ureas, squaramides, and similar NH donor groups.[7-9]

Despite the great potential of CPO, the scarcity of available catalyst families enormously hinders the development of this area (Figure 1A).[1,10-15] Consequently, the number of studies regarding CPO remains far fewer than those of other areas of organocatalysis, and only a few reaction types, such as the aza-Henry,[16-22] Hetero-Diels–Alder,[23] and iodolactonization reactions,[24] have been considered. The main reasons behind the lack of progress in this area are probably related to the high complexity of CPO reactions, which often involve processes with four noncovalent units. In this sense, the absence of a solid mechanistic understanding of CPO delays any attempt to discover or improve new catalysts.

To the best of our knowledge, there have only been a few of computational studies attempting to rationalize the mechanism behind a CPO reaction.[25-29] The results confirm the high complexity of mechanistic studies in this type of catalysis, involving competitions between multiple transition states (TSs) and conformations, and the formation of extensive noncovalent interaction networks. Consequently, there is still an important gap of information regarding reaction mechanisms that needs to be filled to ensure optimal development of CPO reactions (Figure 1B). For example, future research focused on CPO could benefit from experimental kinetic experiments aimed at revealing the rate- and selectivity-determining steps.

Furthermore, a good correlation between computational results, microkinetic simulations, and experimental rates and enantioselectivity is necessary to ensure that state-of-the-art theoretical methods are reliable enough to model CPO systems. These theoretical tools may play a crucial role in revealing elusive reaction details, such as the influence of counterions on enantioselectivity in CPO. Understanding the role of commonly ignored counteranions would uncover new features important for reaction development.

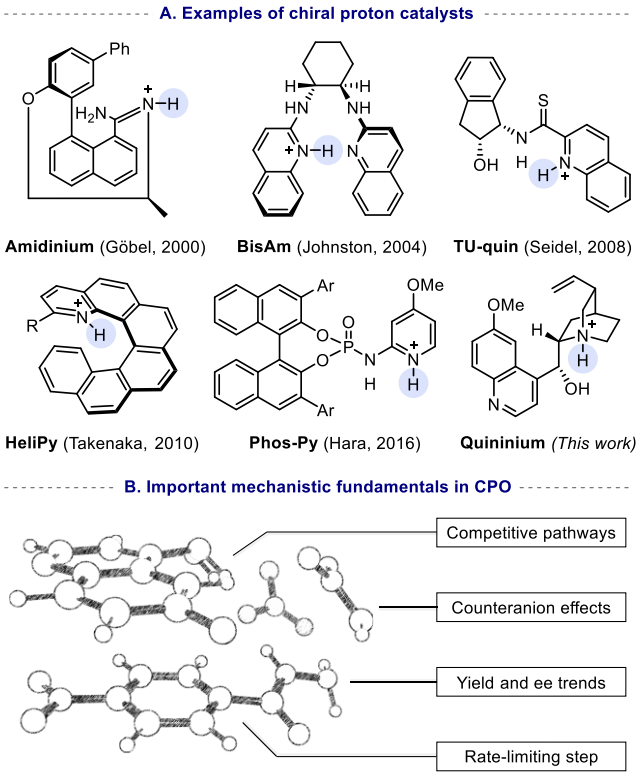


**Figure 1.** (A) Representative examples of CPO families. (B) Important mechanistic features in CPO.

In this study, *N*-protonated cinchonium derivatives are presented as a new family of catalysts for promoting aza-Michael additions. We employ both computational and experimental techniques to comprehensively expand our mechanistic understanding of this type of catalysis. This has the potential to provide valuable insights that can facilitate the development of CPO.

## RESULTS AND DISCUSSION

### Synthesis of catalysts and reaction development

Protonated cinchonium catalysts were prepared using an efficient and straightforward protocol that involves mixing equimolar amounts of cinchona alkaloids and Brønsted acids (Scheme 1). The catalysts can be obtained by evaporating the solvent and the synthetic method was compatible with different cinchona derivatives, such as quinine (**QN**, **1**) and cinchonidine (**CD**, **2**), and acids (**a-d**). The synthesis of the catalysts was confirmed through monocrystal X-ray diffraction analysis using **2b**, which revealed the presence of protonated quinuclidine groups in the cinchona derivatives.[30]

The catalysts were tested in the target aza-Michael addition of hydrazides **3** to nitrostyrene derivatives **4**. After an extensive screening of reaction conditions, it was determined that the optimal conditions included catalyst **1d** and hydrazide **3c**, using $CH_2Cl_2$ as the solvent at −27 °C (Table S1). Additional tests were performed using individually **1**, benzoic acid, and sodium benzoate as catalysts for the reactions (Table S1, entries 27-29).

**Scheme 1. Synthesis of cinchonium derivatives 1a-d and 2a-c and X-ray structure of compound 2b.**

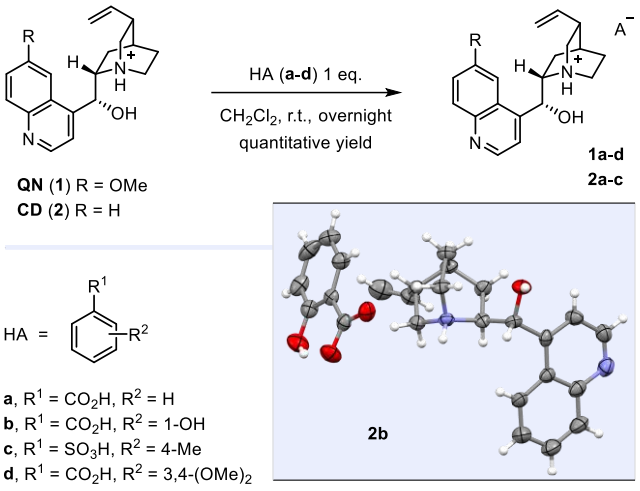


The unsuccessful results obtained suggest that both parts of the cinchonium salts are necessary to promote optimal reactivity and enantioselectivity. Furthermore, the nuclear magnetic resonance (NMR) spectra of catalysts **1** and **2** indicate that their quinuclidine groups remain protonated in solution (Figure S9).

As shown in Scheme 2, the aza-Michael addition was successfully implemented using different nitroalkenes **4**. In most cases, the final products **5** were obtained with excellent yields and good enantio-meric excesses (ee). As a general trend, the data suggests that the yield and ee increase as the nitroalkene acceptor becomes more electron-withdrawing (78 to >95% yield in **5ca-cg** *vs* 54 to 77% yield in **5ch-cj**). The absolute configuration of adducts **5** was determined to be *R* based on previous data.[31]

**Scheme 2. Scope of the aza-Michael reaction catalyzed by 1d.**

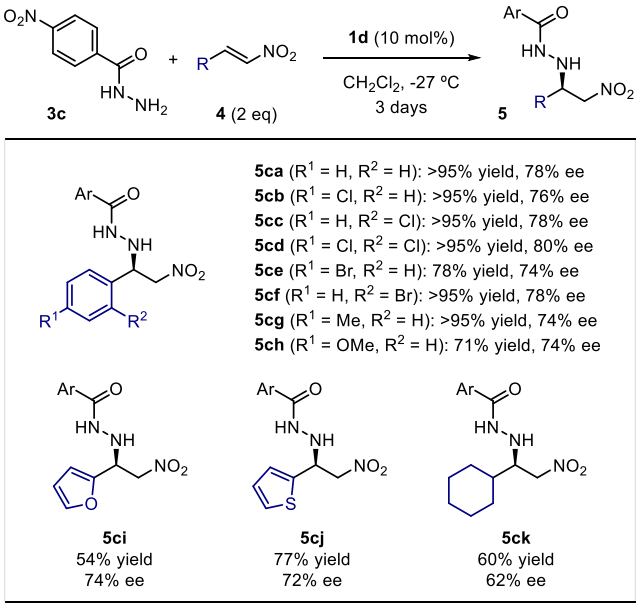

## Computational mechanistic study

We first employed computational techniques to investigate the reaction mechanism using **1a**, **3c**, and **4a**. We modeled catalyst **1a** since this structure does not contain the two methoxy groups of **1d** while giving very similar yield and ee (Table S1, entries 23 and 24 *vs* 30 and 31). Multiple competitive pathways and activation modes were considered (Figures 2 and S45, and Table S6), as well as an extensive conformational space[32] (see the *Conformational sampling* section of the ESI for more details).

Due to the differences in energy observed when varying the level of theory, we opted to include various DFT and wavefunction theory methods.[33-35] Figure 2 displays the average values and standard deviations of six combinations of widely-used functionals and basis sets in modern mechanistic studies (methods A to F). *A priori*, it was not possible to select a single method from the six available based on their benchmarking against experimental results (Tables S4-5). To account for discrepancies between methods, we used the average G values of all six methods, as the choice of theory level is typically an arbitrary decision that depends on the practices of individual research groups. For example, variations as high as 9.5 kcal·mol$^{-1}$ in the relative Gibbs free energy (ΔG) values were observed (i.e., ΔG is 4.9 and −4.6 for (*R*)-**Int-III** for methods C and F, respectively), but the shapes of the energy profiles remained similar across all methods.

The reaction proceeds through a relatively complex mechanism involving four noncovalently attached components. Reaction pathways containing four interacting units are rare in organocatalytic mechanistic studies,[36-40] typically only containing noncovalent catalytic clusters with up to three units of catalyst and substrate. The mechanism begins with the exergonic formation of the catalyst···hydrazide (**1a**···**3c**) and catalyst···hydrazide···nitrostyrene complexes (**Int-I**, Figure 2).

Subsequently, the hydrazide nucleophile attacks nitrostyrene ((*R*)-**TS-I**), leading to the creation of the *R* stereocenter. Then, a rapid proton transfer occurs between the intermediate Michael adduct and the benzoate anion (from (*R*)-**Int-II** to (*R*)-**Int-III**), followed by the protonation of the intermediate adduct in (*R*)-**TS-III**. The most stable species of the profile, the noncovalent catalyst···product complex observed in (*R*)-**Int-IV**, might cause catalyst inhibition as product (*R*)-**5ca** is generated. This effect has been previously observed in other cinchona-catalyzed reactions,[41] suggesting that it might not be a rare event in catalysis with cinchona derivatives.

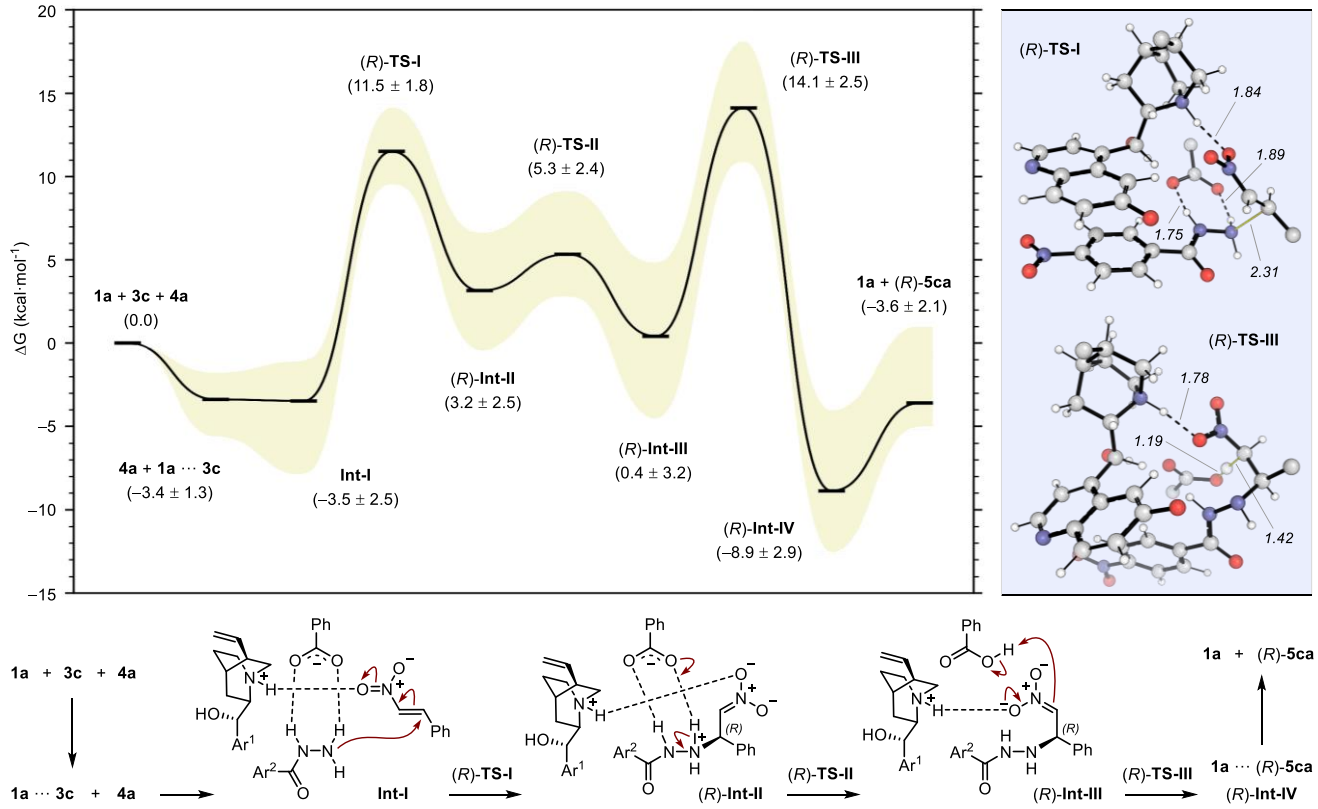


**Figure 2.** Energy profile using Boltzmann weighted ΔG values (in kcal·mol$^{-1}$) with catalyst **1a**, 4-nitrophenylhydrazine (**3c**), *trans*-β-nitrostyrene (**4a**), Ar$^1$ = (6-methoxyquinoline-4-yl); Ar$^2$ = 4-NO$_2$-phenyl. Representations of the most stable conformers found in (*R*)-**TS-I** and (*R*)-**TS-III** with method B are also included. The most relevant H bonds are included as dotted black lines and bonds involved in the TSs are shown as thin yellow lines. Distances are included in Å. Quasi-harmonic (QHA) vibrational, 1 M standard state and conformational entropy corrections were computed and applied by the *GoodVibes*[42] program at –27 °C (246.15 K). The SMD solvation model with dichloromethane[43-48] was included in all the calculations. The six levels of theory used include a geometry optimization at the ωB97X-D[49-50]/6-31+G(d,p) level[51-56] and single-point energy corrections from (A) ωB97X-D/Def2-QZVPP,[57-58] (B) M06-2X-D3[59-60]/Def2-QZVPP, (C)

B3LYP-D3(BJ)[61-64]/Def2-QZVPP, (D) ωB97X-D/6-311++G(2df,p), (E) ωB97X-D/aug-cc-pVTZ, (F) DLPNO-CCSD(T)[65-68]/cc-pV(DT)Z.[69-70] The yellow area represents the range of possible values of the six methods.

The computational mechanism revealed an important interaction between the acidic quinuclidinium group and nitroalkenes **4**, which is likely the main activating interaction of the electrophiles during the (*R*)-**TS-I** addition. This interaction is also present in all the TSs of the reaction. Additionally, the results suggest that the benzoate counteranion forms H bonds that aid the nucleophilic attack of **3c** during the addition.

## Experimental mechanistic study and validation of computational results

The theoretical results obtained are crucial to understand the mechanistic characteristics of the reaction. However, this computational insight has some limitations and requires experimental validation to ensure the validity of the proposed mechanism. One of the most important features to study through experimental kinetic experiments is the position of the rate-limiting step (RLS), as computational results show two potential candidates that are relatively close in energy (ΔG of 11.5 ± 1.8 *vs* 14.1 ± 2.5 kcal·mol$^{-1}$ for (*R*)-**TS-I** and (*R*)-**TS-III**, respectively). Relying exclusively on these theoretical results to determine the RLS may be questionable due to the small energy difference between the two steps.

Therefore, the RLS was determined experimentally using different kinetic techniques. First, two deuterated nitrostyrene compounds were synthesized, which contained the D atom in different positions (Figure 3, top). These deuterated compounds were designed to show specific kinetic isotope effects (KIEs) in one of the two possible RLSs. For example, **4a-β-D** contains the D atom in the position receiving the nucleophilic attack in **TS-I**, and thus, its neighboring C atom undergoes a hybridization change from sp$^2$ to sp$^3$, which is associated with inverse secondary KIEs.[71] Indeed, a secondary KIE effect in **TS-I** is observed in the calculated value (0.95)[72] using DFT frequency information. The experimental values showed secondary KIE effects ranging from 0.85 to 0.94 based on three measurements in **4a-β-D**, suggesting that **TS-I** is the RLS.

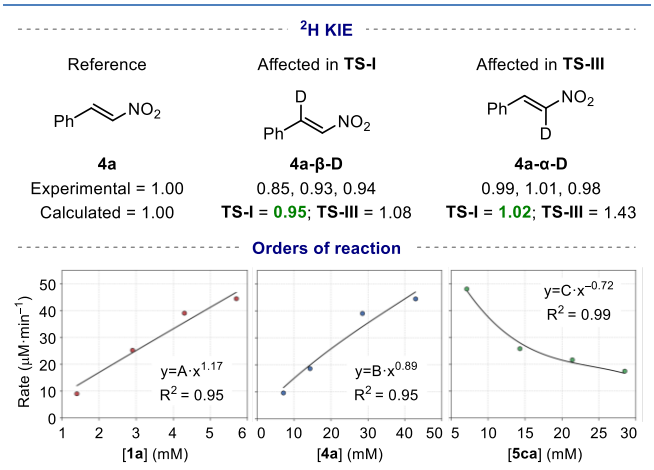


**Figure 3.** Experimentally observed KIEs (top) and orders of reaction (bottom).

In contrast, the calculated KIE (1.02) of **4a-α-D** in (*R*)-**TS-I** is close to one, whereas the value in (*R*)-**TS-III** should be much larger (calculated 1.43). The experimental results showed non-existent KIEs in this case (0.99, 1.01 and 0.98, Figure 3, top), supporting the notion that **TS-I** is the RLS of the process. The absence of D/H exchange in the **5ca-α-D** product indicates that the reaction is not reversible and the ee is determined in the RLS **TS-I**, implying kinetic control. This finding also supports the presence of an intermediate (**Int-IV**) after **TS-I** that is more stable than the resting state (**Int-I**), which makes the reverse reaction irreversible.

Overall, these results emphasize the importance of experimental validation when studying CPO mechanisms and avoiding drawing conclusions based solely on fully computational reaction profiles. For example, in this study, most theoretical methods predicted **TS-III** to be the RLS, while experimental validation revealed **TS-I** as the RLS. This discrepancy is likely caused by the inherent uncertainty in computational results when modeling complex catalytic systems that involve extensive noncovalent networks.

We then measured the orders of reaction (Figure 3, bottom) to ensure proper design of the reaction pathways, in which only one molecule of each component is modeled. The order of reaction was measured for **1a** and **4a**, showing approximately order of one for each compound (1.17 and 0.89 for **1a** and **4a**, respectively) and matching the computational approaches. The negative order observed for **5ca** (–0.72) indicates that the reaction rate decreases as this product forms. This result is consistent with the favorable formation of complex **1a**···(*R*)-**5ca** observed in the computational profile ((*R*)-**Int-IV**, –8.9 kcal·mol$^{-1}$, Figure 2).

Additionally, different titration experiments were carried out to further validate the theoretical results. The addition of catalyst **1a** over a homogeneous solution of reagent **3c** results in significant peak shifts of the CONH group, even after the addition of only 0.2 eq of **1a** (from 7.49 to 7.72 ppm, Figure 4A). This shift is accompanied by subtler movements of other signals, such as those from aromatic H atoms (from 8.29 to 8.06 after the addition of 10 eq of **1a**). Both shifts are consistent with the computational results that suggest the formation of a favorable resting state through catalyst···reagent noncovalent complexation (**4a** + **1a**···**3c**, –3.4 kcal·mol$^{-1}$, Figure 2). Furthermore, the shifts observed during the addition of **1a** to product (*R*)-**5ca** (Figure 4B) support the predicted increase in catalyst inhibition over the course of the reaction, attributed to the favorable formation of a catalyst···product complex ((*R*)-**Int-IV**, –8.9 kcal·mol$^{-1}$, Figure 2).

After validating the proposed energy profile through multiple kinetic studies, we focused on the RLS **TS-I** to analyze the main features behind the stereodifferentiation that occurs in this process. The attack favoring the *R* enantiomer shows a better docking between the quininium cation and nitrostyrene **4a**, activating the electrophile to a greater extent and thereby favoring the formation of this enantiomer (bonds highlighted in red, Figure 5A). On the contrary, the activation of nucleophilic hydrazide

**3c** by the benzoate counteranion remains similar in both competitive TSs (bonds highlighted in blue).

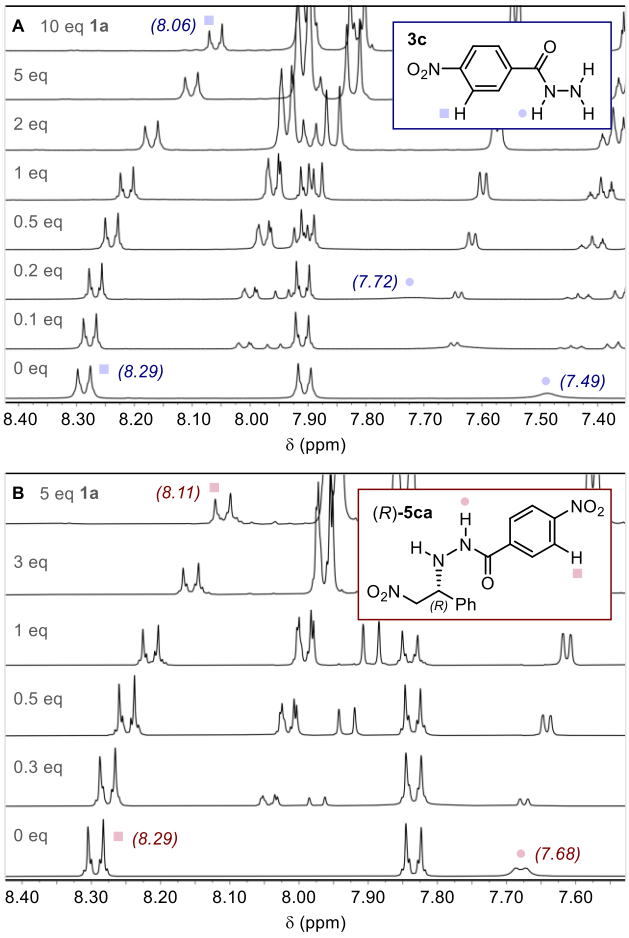


**Figure 4.** Titration experiments adding **1a** over hydrazide **3c** (A) and product (*R*)-**5ca** (B).

This result suggests that the type of benzoate counteranion should not significantly influence ee, which is consistent with the comparable ee values obtained when using different benzoate derivatives (48% *vs* 44% ee for **1a** and **1b**, respectively, Table S1, entries 5 and 6, and 78% ee for both **1a** and **1d**, Table S1, entries 23 and 30).

All of the theoretical methods were able to satisfactorily capture the experimental ee ($\Delta\Delta G^{\ddagger}$ of 1.0 *vs* 1.2 ± 0.4 kcal·mol$^{-1}$, Figure 5B). However, as discussed earlier, we acknowledge that there may be computational limitations and uncertainties, and we cannot completely rule out the possibility of a "lucky outcome" (i.e., since there are only two possible enantiomers, *R* and *S*, it is relatively easy to arrive at the correct result for the wrong reasons).[41]

The calculations suggest that the type of counteranion plays an important role in the reaction since the anions activate the nucleophile in **TS-I**, and therefore, should accelerate the reaction. We further tested this hypothesis experimentally using chloride as the anion (**1e**) since this change should trigger a diminished nucleophile activation caused by the poorer ability of chloride to form H bonds with hydrazide **3c**. As expected, the calculations showed increased activation barriers (15.3 *vs* 17.9 kcal/mol for benzoate and chloride counteranions, respectively, Figure 5B-C), and the experimental yield dropped accordingly (from >95% to <10% for benzoate and chloride, respectively). Overall, these results highlight the importance of understanding reaction mechanisms in CPO to design strategies for counteranion tuning and, consequently, maximizing reactivity and selectivity during reaction development.

A final comparison of yield profiles over time was performed to validate the calculated energy profile. Figure 6 shows that the experimental and predicted curves match well when applying small changes of 1.5 kcal·mol$^{-1}$ to the relative G values (see the *Microkinetic simulations with Berkeley-Madonna* section in the ESI for more details). The good agreement observed in this analysis further strengthens the theoretical mechanism.

## CONCLUSIONS

In summary, we conducted a thorough investigation of a quininium-catalyzed aza-Michael reaction, which furnishes crucial data for developing reactions in CPO. The use of cinchona derivatives as chiral proton catalysts highlights their potential beyond their usual functions as base-promoted and phase-transfer catalysts. We used DFT, wavefunction theory, and microkinetic simulations to model competitive reaction pathways.

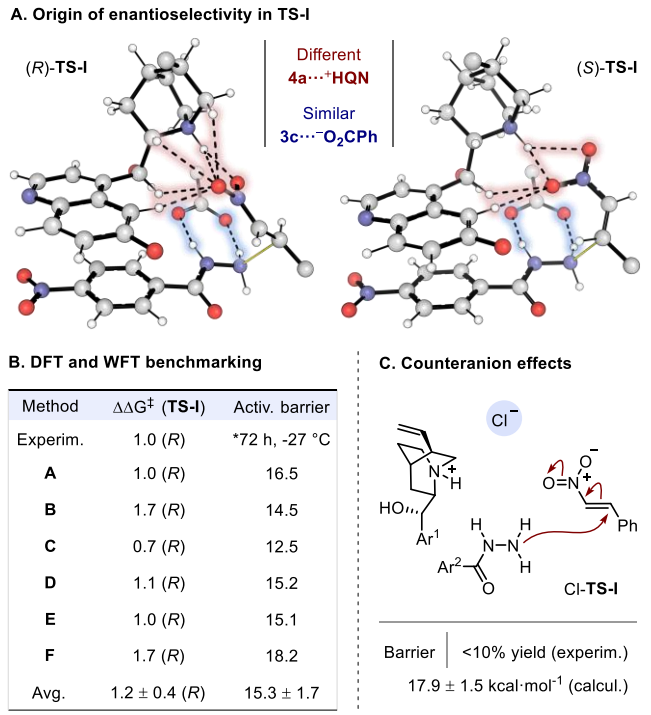


| Method | $\Delta\Delta G^{\ddagger}$ (**TS-I**) | Activ. barrier |
|---|---|---|
| Experim. | 1.0 (*R*) | *72 h, -27 °C |
| **A** | 1.0 (*R*) | 16.5 |
| **B** | 1.7 (*R*) | 14.5 |
| **C** | 0.7 (*R*) | 12.5 |
| **D** | 1.1 (*R*) | 15.2 |
| **E** | 1.0 (*R*) | 15.1 |
| **F** | 1.7 (*R*) | 18.2 |
| Avg. | 1.2 ± 0.4 (*R*) | 15.3 ± 1.7 |

**Figure 5.** (A) Representation of the most stable conformers of (*R*)- and (*S*)-**TS-I** highlighting the most important interactions. (B) $\Delta\Delta G^{\ddagger}$ of **TS-I** enantiomeric pathways and overall activation barriers of the reaction calculated with different methods at –27 °C (246.15 K). (C) Calculated barrier and experimental yield obtained

when using a catalyst with a $Cl^-$ counteranion (**1e**) at –27 °C (246.15 K).

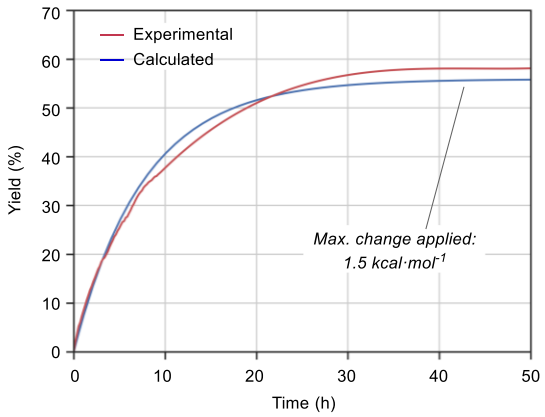


**Figure 6.** Microkinetic simulation of the reaction using the computed averaged energy values *vs* an experimental profile. The reaction conditions were adjusted for NMR conditions and time: 0.01 mmol of **3c**, 0.01 mmol of **4a** and 0.003 mmol of **1a** in 0.6 mL $CD_2Cl_2$, T = 20 °C (293.15 K, G values recalculated at this T).

Different theoretical methods were included due to the high complexity of the mechanism, which involved four non-covalently interacting units. However, the close energy gaps between **TS-I** and **TS-III** made the determination of the RLS uncertain when relying solely on calculated results.

Theoretical studies were complemented with experimental titration and kinetic techniques, which revealed that the rate- and selectivity-determining step was the hydrazide addition presented in **TS-I**. The experimental orders of reaction, with a value of one measured for **1a** and **4a**, reinforced the computational reaction profile used. Additionally, the negative order of reaction displayed by product **5ca** is in line with the favorable energy shown by **Int-IV** in the computational reaction profile. Further titration experiments provided additional support for this proposal.

The computational results suggest that a more efficient substrate docking favors the *R* enantiomer in the selectivity-determining step **TS-I**. Computational and experimental tests also demonstrate how carboxylic counterions are crucial in understanding reaction yield and enantioselectivity, as they act as nucleophile-activating bases. Overall, this research introduces cinchonium derivatives as new options for CPO, accompanied by a comprehensive mechanistic study that could potentially broaden the scope of this underexplored area of catalysis.

## AUTHOR INFORMATION


### Corresponding Authors

* jv.alegre@csic.es
* raquelph@unizar.es


### Author Contributions

All authors have given approval to the final version of the manuscript.

### Notes

The authors declare no competing financial interest.

## ACKNOWLEDGMENT


The authors thank Agencia Estatal de Investigación (AEI), projects PID2019-104379RB-C21 and PID2020-117455GB-I00/AEI/10.13039/501100011033, and Gobierno de Aragón-Fondo Social Europeo (Research Group E07_23R). J.V.A.-R. acknowledges financial support through a Juan de la Cierva Incorporación contract from the Ministry of Science and Innovation (MCIN) and the State Research Agency (AEI) of Spain, and the European Union (NextGenerationEU/PRTR) under grant reference IJC2020-044217-I. J.V.A.-R. acknowledges the computing resources at the Galicia Supercomputing Center, CESGA, including access to the FinisTerrae supercomputer, the Red Española de Supercomputación (grant number QH-2023-1-0003) and the Drago cluster facility of SGAI-CSIC.


## REFERENCES


(1) Nugent, B. M.; Yoder, R. A.; Johnston, J. N. Chiral proton catalysis: a catalytic enantioselective direct aza-Henry reaction. *J. Am. Chem. Soc.* **2004**, *126*, 3418–3419.

(2) Akiyama, T. Stronger Brønsted acids. *Chem. Rev.* **2007**, *107*, 5744–5758.

(3) Kampen, D.; Reisinger, C. M.; List, B. Chiral Brønsted Acids for Asymmetric Organocatalysis. *Top. Curr. Chem.* **2010**, *291*, 395–456.

(4) Schenker, S.; Zamfir, A.; Freund, M.; Tsogoeva, S. B. Developments in Chiral Binaphthyl-Derived Brønsted/Lewis Acids and Hydrogen-Bond-Donor Organocatalysis. *Eur. J. Org. Chem.* **2011**, 2209–2222.

(5) Parmar, D.; Sugiono, E.; Raja, S.; Rueping, M. Complete field guide to asymmetric BINOL-phosphate derived Brønsted acid and metal catalysis: history and classification by mode of activation; Brønsted acidity, hydrogen bonding, ion pairing, and metal phosphates. *Chem. Rev.* **2014**, *114*, 9047–9153.

(6) Min, C.; Seidel, D. Asymmetric Brønsted acid catalysis with chiral carboxylic acids. *Chem. Soc. Rev.* **2017**, *46*, 5889–5902.

(7) Hess, A. S.; Yoder, R. A.; Johnston, J. N. Chiral Proton Catalysis: $pK_a$ Determination for a BAM-HX Brønsted Acid. *Synlett* **2006**, 147–149.

(8) Jakab, G.; Tancon, C.; Zhang, Z.; Lippert, K. M.; Schreiner, P. R. (Thio)urea Organocatalyst Equilibrium Acidities in DMSO. *Org. Lett.* **2012**, *14*, 1724–1727.

(9) Ni, X.; Li, X.; Wang, Z.; Cheng, J.-P. Squaramide Equilibrium Acidities in DMSO. *Org. Lett.* **2014**, *16*, 1786–1789.

(10) Schuster, T.; Bauch, M.; Dürner, G.; Göbel, M. W. Axially Chiral Amidinium Ions as Inducers of Enantioselectivity in Diels-Alder Reactions. *Org. Lett.* **2000**, *2*, 179−181.

(11) Ganesh, M.; Seidel, D. Catalytic Enantioselective Additions of Indoles to Nitroalkenes. *J. Am. Chem. Soc.* **2008**, *130*, 16464−16465.

(12) Yoshida, K.; Inokuma, T.; Takasu, K.; Takemoto, Y. Catalytic asymmetric synthesis of both enantiomers of 4-substituted 1,4-dihydropyridines with the use of bifunctional thiourea-ammonium salts bearing different counterions. *Molecules* **2010**, *15*, 8305−8326.

(13) Takenaka, N.; Chen, J.; Captain, B.; Sarangthem, R. S.; Chandrakumar, A. Helical chiral 2-aminopyridinium ions: A new class of hydrogen bond donor catalysts. *J. Am. Chem. Soc.* **2010**, *132*, 4536−4537.

(14) Chen, W.; Yang, W.; Yan, L.; Tan, C.-H.; Jiang, Z. Bicyclic guanidinium-catalyzed enantioselective phase-transfer alkylation: Direct access to pyrroloindolines and furoindolines. *Chem. Commun.* **2013**, *49*, 9854−9856.

(15) Nishikawa, Y.; Nakano, S.; Tahira, Y.; Terazawa, K.; Yamazaki, K.; Kitamura, C.; Hara, O. Chiral pyridinium phosphoramide as a dual Brønsted acid catalyst for enantioselective Diels–Alder reaction. *Org. Lett.* **2016**, *18*, 2004−2007.

(16) Singh, A.; Yoder, R. A.; Shen, B.; Johnston, J. N. Chiral Proton Catalysis: Enantioselective Brønsted Acid Catalyzed Additions of Nitroacetic Acid Derivatives as Glycine Equivalents. *J. Am. Chem. Soc*. **2007**, *129*, 3466–3467.

(17) Wilt, J. C.; Pink, M.; Johnston, J. N. A diastereo- and enantioselective synthesis of α-substituted anti-α,β-diaminophosphonic acid derivatives. *Chem. Commun*. **2008**, 4177-4179.

(18) Shen, B.; Johnston, J. N. A Formal Enantioselective Acetate Mannich Reaction: The Nitro Functional Group as a Traceless Agent for Activation and Enantiocontrol in the Synthesis of β-Amino Acids. *Org. Lett*. **2008**, *10*, 4397–4400.

(19) Singh, A.; Johnston, J. N. A Diastereo- and Enantioselective Synthesis of α-Substituted syn-α,β-Diamino Acids. *J. Am. Chem. Soc*. **2008**, *130*, 5866–5867.

(20) Davis, T. A.; Wilt, J. C.; Johnston, J. N. Bifunctional Asymmetric Catalysis: Amplification of Brønsted Basicity Can Orthogonally Increase the Reactivity of a Chiral Brønsted Acid. *J. Am. Chem. Soc*. **2010**, *132*, 2880–2882.

(21) Shen, B.; Makley, D. M.; Johnston, J. N. Umpolung reactivity in amide and peptide synthesis. *Nature* **2010**, *465*, 1027–1032.

(22) Davis, T. A.; Danneman, M. W.; Johnston, J. N. Chiral proton catalysis of secondary nitroalkane additions to azomethine: synthesis of a potent GlyT1 inhibitor. *Chem. Commun*. **2012**, 5578–5580.

(23) Sprague, D. J.; Nugent, B. M.; Yoder, R. A.; Vara, B. A.; Johnston, J. N. Adaptation of a small-molecule hydrogen-bond donor catalyst to an enantioselective hetero-Diels−Alder reaction hypothesized for brevianamide biosynthesis. *Org. Lett.* **2015**, *17*, 880–883.

(24) Dobish, M. C.; Johnston, J. N. Achiral counterion control of enantioselectivity in a Brønsted acid-catalyzed iodo-lactonization. *J. Am. Chem. Soc.* **2012**, *134*, 6068–6071.

(25) Belding, L.; Taimoory, S. M.; Dudding, T. Mirroring Enzymes: The Role of Hydrogen Bonding in an Asymmetric Organocatalyzed Aza-Henry Reaction - a DFT Study. *ACS Catal.* **2015**, *5*, 343−349.

(26) Taimoory, S. M.; Dudding, T. An Evolving Insight into Chiral H-Bond Catalyzed Aza-Henry Reactions: A Cooperative Role for Noncovalent Attractive Interactions Unveiled by Density Functional Theory. *J. Org. Chem.* **2016**, *81*, 3286−3295.

(27) Nájera, C.; Sansano, J. M.; Gómez-Bengoa, E. Heterocycle-based bifunctional organocatalysts in asymmetric synthesis. *Pure Appl. Chem.* **2016**, *88*, 561−578, and references therein.

(28) Struble, T. J.; SmaJlagic, I.; Foy, H.; Dudding, T.; Johnston, J. N. DFT-Based Stereochemical Rationales for the Bifunctional Brønsted Acid/Base-Catalyzed Diastereodivergent and Enantioselective aza-Henry Reactions of α-Nitro Esters. *J. Org. Chem.* **2021**, *86*, 15606−15617.

(29) Smajlagic, I.; Johnston, J. N.; Dudding, T. Secondary Orbital Effect Involving Fluorine is Responsible for Substrate-Controlled Diastereodivergence in the Catalyzed *syn*-aza-Henry Reaction of α-Fluoronitroalkanes. *Chem. Eur. J.* **2023**, *29*, e202204066.

(30) CCDC-2098237 (**2b**) Contains the Supplementary crystallographic Data for This Paper. These Data can be Obtained Free of Charge via http://www.ccdc.cam.ac.uk/conts/retrieving.html (or from the CCDC, 12 Union Road, Cambridge CB2 1EZ, UK; Fax: +44 1223 336033; E-mail: deposit@ccdc.cam.ac.uk).

(31) Alcaine, A.; Marqués-López, E.; Herrera, R. P. Synthesis of Interesting β-Nitrohydrazides through Thiourea Organocatalyzed aza-Michael Addition. *RSC Adv.* **2014**, *4*, 9856–9865.

(32) Grimme, S. Exploration of Chemical Compound, Conformer, and Reaction Space with Meta-Dynamics Simulations Based on Tight-Binding Quantum Chemical Calculations. *J. Chem. Theory Comput.* **2019**, *15*, 2847–2862.

(33) Gaussian 16, Revision B.01, Gaussian, Inc., Wallingford CT, 2016 (full reference available in the ESI).

(34) AQME, version 1.3.0, Alegre-Requena, J. V.; Sowndarya, S.; Alturaifi, T.; Pérez-Soto, R.; Paton, R. S. AQME: Automated Quantum Mechanical Environments for Researchers and Educators. *Wiley Interdiscip. Rev. Comput. Mol. Sci.* **2023**, https://doi.org/10.1002/wcms.1663.

(35) ORCA, version 4.2.1, Neese, F. The ORCA Program System. *Wiley Interdiscip. Rev. Comput. Mol. Sci.* **2012**, *2*, 73–78.

(36) Maeda, S.; Komagawa, S.; Uchiyama, M.; Morokuma, K. Finding Reaction Pathways for Multicomponent Reactions: The Passerini Reaction is a Four-Component Reaction. *Angew. Chem. Int. Ed.* **2011**, *50*, 644–649.

(37) Ramozzi, R.; Morokuma, K. Revisiting the Passerini Reaction Mechanism: Existence of the Nitrilium, Organocatalysis of Its Formation, and Solvent Effect. *J. Org. Chem.* **2015**, *80*, 5652–5657.

(38) Park, Y.; Harper, K. C.; Kuhl, N.; Kwan, E. E.; Liu, R. Y.; Jacobsen, E. N. Macrocyclic bis-thioureas catalyze stereospecific glycosylation reactions. *Science* **2017**, *355*, 162–166.

(39) Xie, M.-S.; Huang, B.; Li, N.; Tian, Y.; Wu, X.-X.; Deng, Y.; Qu, G.-R.; Guo, H.-M. Rational Design of 2-Substituted DMAP-N-oxides as Acyl Transfer Catalysts: Dynamic Kinetic Resolution of Azlactones. *J. Am. Chem. Soc.* **2020**, *142*, 19226−19238.

(40) Gómez-Torres, E.; Alonso, D. A.; Gómez-Bengoa, E.; Nájera, C. Enantioselective Synthesis of Succinimides by Michael Addition of 1,3-Dicarbonyl Compounds to Maleimides Catalyzed by a Chiral Bis(2-aminobenzimidazole) Organocatalyst. *Eur. J. Org. Chem.* **2013**, 1434–1440.

(41) Sonsona, I. G.; Alegre-Requena, J. V.; Marqués-López, E.; Gimeno, M. C.; Herrera, R. P. Asymmetric organocatalyzed aza-Henry reaction of hydrazones: experimental and computational studies. C*hem. Eur. J.* **2020**, *26*, 5469–5478.

(42) GoodVibes v3.0.2, Luchini, G.; Alegre-Requena, J. V.; Funes-Ardoiz, I.; Paton, R. S. GoodVibes: Automated Thermochemistry for Heterogeneous Computational Chemistry Data. *F1000Research* **2020**, *9*, 291.

(43) Cancès, E.; Mennucci, B.; Tomasi, J. A new integral equation formalism for the polarizable continuum model: Theoretical background and applications to isotropic and anisotropic dielectrics. *J. Chem. Phys.* **1997**, *107*, 3032–3041.

(44) Mennucci, B.; Cancès, E.; Tomasi, J. Evaluation of solvent effects in isotropic and anisotropic dielectrics and in ionic solutions with a unified integral equation method: theoretical bases, computational implementation, and numerical applications. *J. Phys. Chem. B.* **1997**, *101*, 10506–10517.

(45) Mennucci, B.; Tomasi, J. Continuum solvation models: A new approach to the problem of solute's charge distribution and cavity boundaries. *J. Chem. Phys.* **1997**, *106*, 5151–5158.

(46) Tomasi, J.; Mennucci, T. B.; Cancès, E. The IEF version of the PCM solvation method: an overview of a new method addressed to study molecular solutes at the QM ab initio level. *J. Mol. Struct. THEOCHEM* **1999**, *464*, 211–226.

(47) Scalmani, G.; Frisch, M. J. Continuous surface charge polarizable continuum models of solvation. I. General formalism. *J. Chem. Phys.* **2010**, *132*, 114110.

(48) Marenich, A. V.; Cramer, C. J.; Truhlar, D. G. Universal solvation model based on solute electron density and on a continuum model of the solvent defined by the bulk dielectric constant and atomic surface tensions. *J. Phys. Chem. B.* **2009**, *113*, 6378–6396.

(49) Becke, A. D. Density-functional thermochemistry. V. Systematic optimization of exchange-correlation functionals. *J. Chem. Phys*. **1997**, *107*, 8554–8560.

(50) Chai, J.-D.; Head-Gordon, M. Long-range corrected hybrid density functionals with damped atom–atom dispersion corrections. *Phys. Chem. Chem. Phys*. **2008**, *10*, 6615–6620.

(51) Hehre, W. J.; Ditchfield, R.; Pople, J. A. Self-consistent molecular orbital methods. XII. Further extensions of gaussian-type basis sets for use in molecular orbital studies of organic molecules. *J. Chem. Phys*. **1972**, *56*, 2257–2261.

(52) Hariharan, P. C.; Pople, J. A. The influence of polarization functions on molecular orbital hydrogenation energies. *Theoret. Chim. Acta* **1973**, *28*, 213–222.

(53) Krishnan, R.; Binkley, J. S.; Seeger, R.; Pople, J. A. Self-consistent molecular orbital methods. XX. A basis set for correlated wave functions. *J. Chem. Phys.* **1980**, *72*, 650–654.

(54) McLean, A. D.; Chandler, G. S. Contracted Gaussian basis sets for molecular calculations. I. Second row atoms, Z=11–18. *J. Chem. Phys.* **1980**, *72*, 5639–5648.

(55) Francl, M. M.; Pietro, W. J.; Hehre, W. J.; Binkley, J. S.; Gordon, M. S.; DeFrees, D. J.; Pople, J. A. Self-consistent molecular orbital methods. XXIII. A polarizationtype basis set for second-row elements. *J. Chem. Phys*. **1982**, *77*, 3654–3665.

(56) Rassolov, V. A.; Ratner, M. A.; Pople, J. A.; Redfern, P. C.; Curtiss, L. A. 6–31G* basis set for thirdrow atoms. *J. Comp. Chem*. **2001**, *22*, 976–984.

(57) Weigend, F.; Ahlrichs, R. Balanced basis sets of split valence, triple zeta valence and quadruple zeta valence quality for H to Rn: Design and assessment of accuracy. *Phys. Chem. Chem. Phys.* **2005**, *7*, 3297−3305.

(58) Weigend, F. Accurate coulomb-fitting basis sets for H to Rn. *Phys. Chem. Chem. Phys.* **2006**, *8*, 1057−1065.

(59) Zhao, Y.; Truhlar, D. G. The M06 suite of density functionals for main group thermochemistry, thermochemical kinetics, noncovalent interactions, excited states, and transition elements: two new functionals and systematic testing of four M06-class functionals and 12 other functionals. *Theor. Chem. Acc.* **2008**, *120*, 215–241.

(60) Grimme, S.; Antony, J.; Ehrlich, S.; Krieg, H. A. Consistent and accurate ab initio parameterization of density functional dispersion correction (DFT-D) for the 94 Elements H-Pu. *J. Chem. Phys.* **2010**, *132*, 154104.

(61) Vosko, S. H.; Wilk, L.; Nusair, M. Accurate spin-dependent electron liquid correlation energies for local spin density calculations: a critical analysis. *Can. J. Phys.* **1980**, *58*, 1200–1211.

(62) Becke, A. D. Density-functional thermochemistry. III. The role of exact exchange. *J. Chem. Phys.* **1993**, *98*, 5648–5652.

(63) Lee, C.; Yang, W.; Parr, R. G. Development of the Colle-Salvetti correlation-energy formula into a functional of the electron density. *Phys. Rev. B* **1988**, *37*, 785–789.

(64) Stephens, P. J.; Devlin, F. J.; Chabalowski, C. F.; Frisch, M. J. Ab Initio Calculation of Vibrational Absorption and Circular Dichroism Spectra Using Density Functional Force Fields. *J. Phys. Chem.* **1994**, *98*, 11623–11627.

(65) Purvis III, G. D.; Bartlett, R. J. A Full Coupled-cluster singles and doubles model: the inclusion of disconnected triples. *J. Chem. Phys.* **1982**, *76*, 1910–1918.

(66) Pople, J. A.; Head-Gordon, M.; Raghavachari, K. Quadratic configuration interaction. A general technique for determining electron correlation energies. *J. Chem. Phys.* **1987**, *87*, 5968–5975.

(67) Riplinger, C.; Neese, F. An efficient and near linear scaling pair natural orbital based local coupled cluster method. *J. Chem. Phys.* **2013**, *138*, 034106.

(68) Riplinger, C.; Pinski, P.; Becker, U.; Valeev, E. F.; Neese, F. Sparse maps – a systematic infrastructure for reduced-scaling electronic structure methods. II. Linear scaling domain based pair natural orbital coupled cluster theory. *J. Chem. Phys.* **2016**, *144*, 024109.

(69) Dunning Jr, T. H. Gaussian basis sets for use in correlated molecular calculations. I. The Atoms boron through neon and hydrogen. *J. Chem. Phys.* **1989**, *90*, 1007–1023.

(70) Woon, D. E.; Dunning Jr, T. H. Gaussian basis sets for use in correlated molecular calculations. III. The Atoms aluminum through argon. *J. Chem. Phys.* **1993**, *98*, 1358–1371.

(71) Alegre-Requena, J. V.; Marqués-López, E.; Herrera, R. P. Optimizing Accuracy and Computational Cost in Theoretical Squaramide Catalysis: The Henry Reaction. *Chem. Eur. J.* **2017**, *23*, 15336–15347.

(72) KINISOT, version 2.0.1 (Python adapted). Paton, R. S. 10.5281/zenodo.6831009, 2022.